

# Investigation on surface morphology and crystalline phase deformation of $\text{Al}_{80}\text{Li}_5\text{Mg}_5\text{Zn}_5\text{Cu}_5$ high-entropy alloy by ultra-precision cutting

Zhiyuan Huang<sup>a</sup>, Yuqi Dai<sup>a</sup>, Zhen Li<sup>a</sup>, Guoqing Zhang<sup>a</sup>, Chuntao Chang<sup>b,c</sup>, Jiang Ma<sup>a,\*</sup>

<sup>a</sup> College of Mechatronics and Control Engineering, Shenzhen University, Shenzhen 518060, China

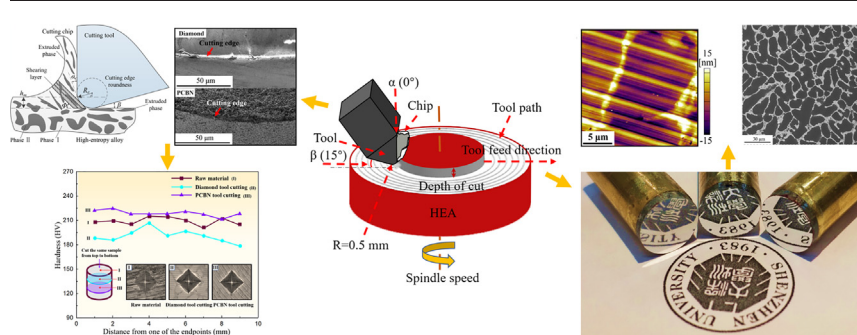
<sup>b</sup> School of Mechanical Engineering, Dongguan University of Technology, Dongguan 523808, China

<sup>c</sup> Neutron Scattering Technical Engineering Research Center, Dongguan University of Technology, China

## HIGHLIGHTS

- The mechanism of ultra-precision machining of HEAs has been deeply studied.
- The effects of spindle speed, feed rate and depth of cut on high-entropy alloy surface quality have been investigated for the first time.
- Two distinct phases with different deformation homogeneous distribute on the HEA surface by ultra-precision machining.

## GRAPHICAL ABSTRACT



## ARTICLE INFO

### Article history:

Received 23 September 2019

Received in revised form 8 November 2019

Accepted 14 November 2019

Available online 16 November 2019

### Keywords:

$\text{Al}_{80}\text{Li}_5\text{Mg}_5\text{Zn}_5\text{Cu}_5$  high-entropy alloy

Ultra-precision cutting

Surface quality

Morphology

Microhardness

## ABSTRACT

The materials with high precision, easy machining and excellent micro-machinability are considered significant on the fabrication of precision components, the outstanding comprehensive properties of  $\text{Al}_{80}\text{Li}_5\text{Mg}_5\text{Zn}_5\text{Cu}_5$  high-entropy alloy just meet these requirements. Firstly, our study found that the feed rate parameters have the greatest influence on the surface quality of material, and the surface roughness can reach 6 nm at the lowest level. After ultra-precision cutting the material, we found that the cutting process of high-entropy alloy has no obvious damage to the cutting tools and two distinct phases (FCC  $\alpha$ -Al phase and  $\text{Al}/\text{Al}_2\text{Cu}/\text{MgZn}_2$  quaternary eutectics phase) were formed on the finished surface under the observation of scanning electron microscopy. By comparing the size of two phases and the morphology of undeformed chips cut by diamond tool and polycrystalline cubic boron nitride (PCBN) tool, the material surface cut by PCBN tool was subjected to greater extrusion force and friction during machining, leading to more remarkable increase in surface microhardness.

© 2019 The Authors. Published by Elsevier Ltd. This is an open access article under the CC BY-NC-ND license (<http://creativecommons.org/licenses/by-nc-nd/4.0/>).

## 1. Introduction

In the 2000s, high-entropy alloy (HEA) was firstly proposed and defined as alloying more than five elements with the same atomic ratio or

near the same atomic ratio [1,2]. HEA is a kind of disordered solid solution main characterized by chemical disorder [3]. After nearly 20 years of research, it has been found that HEAs are a series of alloys with potential superiority to conventional metal materials in hardness [4], compressive strength [5], fracture toughness [6], thermal stability [7] and other properties [8]. Five characteristics of HEAs are summarized: high temperature stability [9], high toughness at low temperature [10],

\* Corresponding author.

E-mail address: [majiang@szu.edu.cn](mailto:majian@szu.edu.cn) (J. Ma).

anti-irradiation swelling rate [11], sluggish diffusion effect [12], low grain boundary energy and stacking fault energy [13]. The applications of HEAs have been concerned by experts and scholars from all walks of life. As some HEAs have high temperature resistance, corrosion resistance and wear resistance, as well as good plasticity, which makes it easy to make turbine blades. Others have soft magnetism and high resistivity, which have great application potential in high frequency communication devices. It can be used to make high frequency transformers, magnetic cores, loudspeakers, etc. [14]. Although HEAs have many advantages, most of the current studies focus on functions and formation mechanism of materials [15], and little research has been done on the machinability of HEAs, especially the ultra-precision cutting performance of HEAs.

Aluminum alloy is one of the most widely used alloys in the industry, which has been widely used in aircraft envelope, automobile structure components and so on. We choose  $\text{Al}_{80}\text{Li}_5\text{Mg}_5\text{Zn}_5\text{Cu}_5$  HEA as research object, through ultra-precision cutting technology, nano-scale surface roughness products can be obtained [16,17], moreover, the density of  $\text{Al}_{80}\text{Li}_5\text{Mg}_5\text{Zn}_5\text{Cu}_5$  HEA is similar to that of aluminum alloy, but its hardness is higher than that of aluminum alloy. At the same time, The HEA has the characteristics of high corrosion resistance, low density, low grain boundary energy and stacking fault energy, and the existence of eutectic phase makes it has the ability of superplastic deformation in the cutting process, which makes the machining process easier and the tool wear less. Compared with devices made of other alloy materials, HEAs devices have better comprehensive performance [18]. The research is expected to replace the use of traditional aluminum alloy in the industrial field, the research on the ultra-precision cutting performance of this new material can also provide reference for other types of HEA.

Because the thickness of the surface material removed in the micro-cutting process differs greatly from that of the surface material removed in the macro-cutting process, there are also differences in the cutting properties between the micro-cutting process and the macro-cutting process [19]. In this work, we studied the effect of spindle speed, feed rate and depth of cut on surface roughness and morphology of  $\text{Al}_{80}\text{Li}_5\text{Mg}_5\text{Zn}_5\text{Cu}_5$  high-entropy alloy in the ultra-precision cutting with diamond tool and PCBN tool, respectively. Considering the different surface qualities and microstructures of the samples after cutting by two kinds of tools, the mechanisms of surface morphology formation and crystal phase deformation were discussed. Then, the ultra-precision cutting performance of HEA was further studied by observing the surface morphology of cutting tools and the corresponding chip. Finally, the mechanical properties of the finished surfaces were investigated via microhardness testing.

## 2. Experimental method

The  $\text{Al}_{80}\text{Li}_5\text{Mg}_5\text{Zn}_5\text{Cu}_5$  (at.%) HEA rods with a diameter of 10 mm were used for ultra-precision cutting experiments. Firstly, the

experimental platform was set up on an ultra-precision lathe as shown in Fig. 1(a), and the schematic of ultra-precision cutting process as shown in Fig. 1(b). Then, under the different parameters listed in Table 1, we explored the relationship between the machined surface roughness and spindle speed, feed rate and cutting depth by cutting HEA surface with diamond tool and PCBN tool. The machined surface quality was collected by white light interferometer (Bruker-GT-X, American) from the center to the edge of the machined surface, three surface roughness of the same distance and area are taken to observe whether the linear velocity has an impact on the surface. After that, we observed its three-dimensional topography more clearly by atomic force microscopy (AFM, MFP-3D Infinity, Britain) in lightweight mode with a  $20\ \mu\text{m} \times 20\ \mu\text{m}$  area. Next, the microstructure morphology of machined surface of HEA was obtained by scanning electron microscopy (SEM, Phenom-ProX, Netherlands) with low magnification and high magnification, It was found that there are obvious black and white crystal phases on the machined surface, and the sizes of crystal phases on the surface of the HEA machined by two kinds of cutters are different. The elements distribution of the sample and the element composition of two different color regions were analyzed by energy dispersive spectrometer (EDS, Phenom-ProX, Netherlands) it should be mentioned here that because the energy corresponding to the X-ray energy spectrum of lithium is too small, only about 50 eV, EDS cannot distinguish lithium element. At the end of the cutting experiment, the wear of these two kinds of cutting tools and the corresponding undeformed chip morphology were observed by SEM. The phase structure of original sample, the diamond tool cutting chips and the PCBN tool cutting chips at the parameter  $v = 2000\ \text{r/min}$ ,  $f = 5\ \mu\text{m/r}$ ,  $d = 8\ \mu\text{m}$  were collected by X-ray diffractometer (XRD, Rigaku-miniflex600, Japan), then, the crystal phase composition of the processed high entropy alloy surface was analyzed by comparing the diffraction peaks of XRD pattern with the standard PDF card of XRD. Finally, in order to observe the mechanical properties and cutting mechanism of HEA surface processed by different cutting tools, the surface microhardness of sample polished by 2000 mesh sandpaper polishing, cut by diamond tool and PCBN tool was measured by an automatic microhardness tester (FM-ARS900, Japan).

## 3. Results and discussion

### 3.1. Surface quality and topography

Under ideal ductile removal conditions, the surface roughness of HEA after ultra-precision cutting depends on the feed rate of the tool and the radius of the tool tip. The relationship between them can be described as follows [20]:

$$R_a = \frac{f^2}{8R} \quad (1)$$

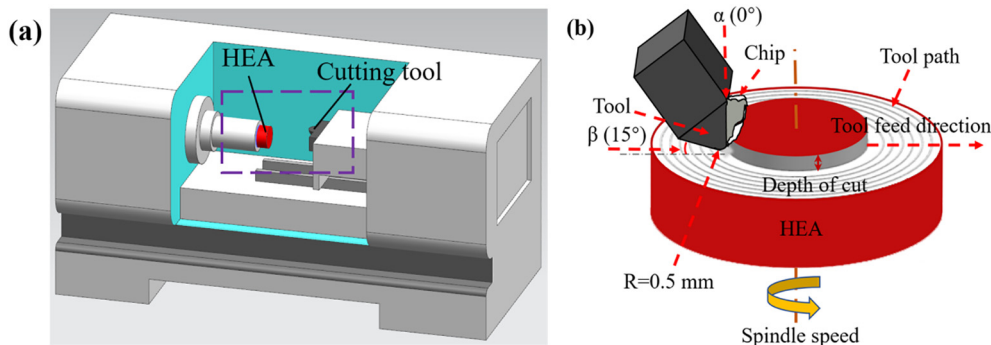
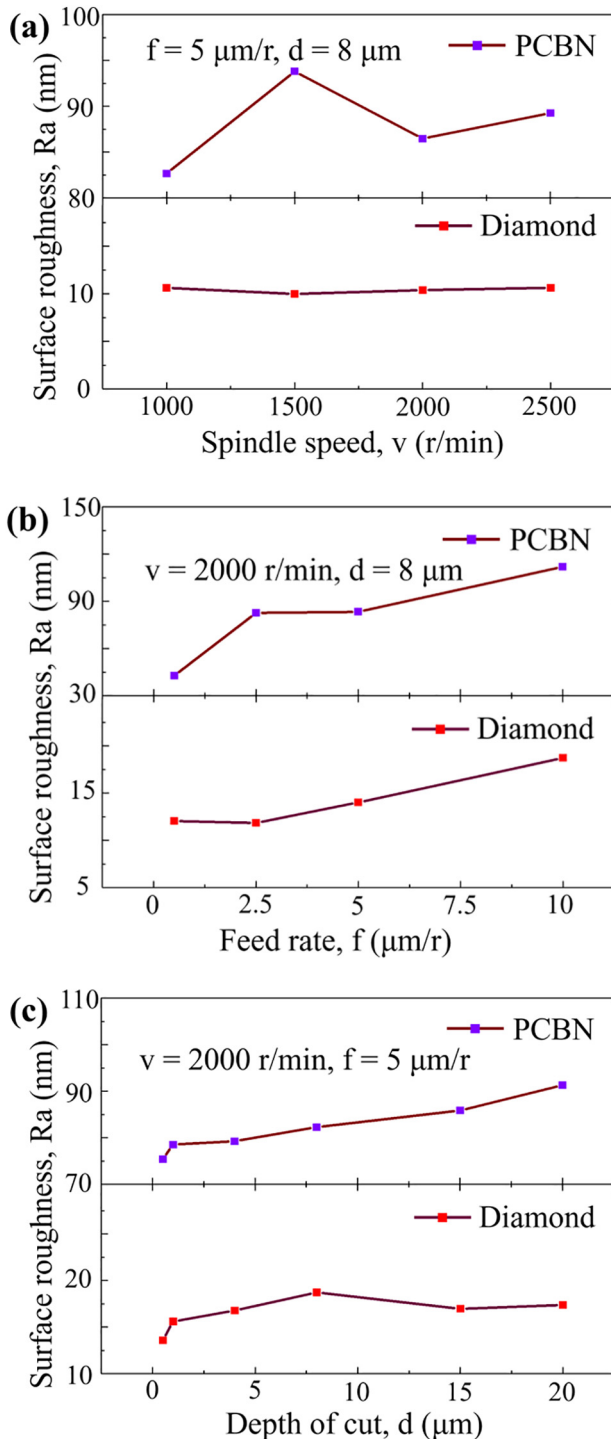


Fig. 1. (a) Experiment setup, the red part is the HEA workpiece and the black part is the cutting tool. (b) The schematic of ultra-precision cutting process.

**Table 1**  
The parameters of ultra-precision cutting.

Name	Value
Tool nose radius ( $R$ )	0.5 mm
Tool rake angle ( $\alpha$ )	0°
Tool clearance angle ( $\beta$ )	15°
Spindle speed ( $v$ )	1000, 1500, 2000, 2500 r/min
Feed rate ( $f$ )	0.5, 2.5, 5, 10 $\mu\text{m/r}$
Depth of cut ( $d$ )	0.5, 1, 4, 8, 15, 20 $\mu\text{m}$



**Fig. 2.** Effect of spindle speed, feed rate and depth of cut on surface roughness of  $\text{Al}_{80}\text{Li}_5\text{Mg}_5\text{Zn}_5\text{Cu}_5$  high-entropy alloy by diamond tool and PCBN tool cutting, respectively.

where  $f$  is the feed rate and  $R$  is the tool nose radius. According to Eq. (1), the theoretical  $R_a$  value is 25 nm which matches the actual value well when the  $f$  is 10  $\mu\text{m/r}$ . Fig. 2 shows the effect of spindle speed, feed rate and cutting depth on surface roughness of HEA after diamond tool and PCBN tool cutting. With the spindle speed from 1000 to 2500 r/min as shown in Fig. 2(a), the  $R_a$  values by diamond tool cutting is basically stable at 10 nm, while the  $R_a$  values by PCBN tool cutting changes little from 83 nm to 89 nm. Fig. 2(b) shows that with the feed rate increasing from 0.5  $\mu\text{m/r}$  to 10  $\mu\text{m/r}$ , the surface roughness by diamond tool cutting changes from 12 nm to 18 nm, and that of PCBN tool cutting changes from 42 nm to 112 nm. With the cutting depth increasing from 0.5  $\mu\text{m}$  to 20  $\mu\text{m}$ , the roughness of the machined surface by diamond tool and PCBN tool cutting changes from 13 to 18 nm and from 75 to 91 nm respectively as shown in Fig. 2(c).

To sum up, excluding the slight effect of tool wear on the  $R_a$  values and the effect of variable cutting speed on the surface roughness is very small, the  $R_a$  increases with the increases of parameter value, and the feed rate has the greatest effect on the surface roughness of HEA in ultra-precision cutting, followed by the cutting depth, while the spindle speed has no significant influence on the surface roughness of HEA.

Under the processing parameters of  $v = 2000 \text{ r/min}, f = 5 \mu\text{m/r}, d = 8 \mu\text{m}$ , the finished surfaces of  $\text{Al}_{80}\text{Li}_5\text{Mg}_5\text{Zn}_5\text{Cu}_5$  HEA cut by diamond tool and PCBN tool all have achieved mirror effect as show in Fig. 3 (a) and (b), among them, the sample 1 was cut by PCBN tool, sample 2 and sample 3 were cut by diamond tool. The surface morphologies cut under the same cutting parameter were obtained by white light interferometer as shown in Fig. 3(c) and (f). The surface roughness of HEA cut by diamond tool and PCBN tool is 18.73 nm and 82.3 nm, respectively. The local enlargement maps of the machined surface morphology are shown in Fig. 3(d) and (g). Selecting a section from it as shown in the red line and the section profile images are showed in Fig. 3(e) and (h). The curves show that the maximum depth of microgrooves machined by diamond tool and PCBN tool is approximately 75 nm and 400 nm, respectively. In order to observe machined surface topography more clearly, the AFM was used to capture its images in lightweight mode and the scanning range of probe is 20  $\mu\text{m} \times 20 \mu\text{m}$ . The surface roughness of diamond tool cutting reaches 6 nm as shown in Fig. 4 (a) and (b), while the surface roughness of PCBN tool cutting is 27 nm as shown in Fig. 4(c) and (d). There are some light and dark stripes in the two-dimensional image, which correspond to the ridges and grooves part of the three-dimensional image, the above surface topography probably caused by the extrusion and viscous flow of high-entropy alloy in ultra-precision cutting process.

### 3.2. Crystalline phase deformation

Fig. 5 shows the XRD patterns of  $\text{Al}_{80}\text{Li}_5\text{Mg}_5\text{Zn}_5\text{Cu}_5$  HEA sample, the HEA chips cut by diamond tool and the HEA chips cut by PCBN tool. The crystal phase composition was analyzed by comparing the diffraction peaks of XRD pattern with the standard PDF card of XRD. It reveals the same diffraction peaks of  $\alpha$ -Al phase,  $\text{Al}_2\text{Cu}$  phase,  $\text{MgZn}_2$  phase and  $\text{Al}_2\text{O}_3$  phase, the intensity of the diffraction peaks of FCC  $\alpha$ -Al phase exceeds that of the other phases, suggesting a predominant volume fraction of  $\alpha$ -Al phase. Moreover, because the composition and phase formation of HEAs are complex, some unknown ternary or even quaternary phases appear [22]. By comparing the XRD patterns of two chips and raw material, some wider peak appears in the XRD pattern of the chips, it shows that the cutting process is squeezed by the cutter and the sample surface, so that the adjacent crystal phases merge into a wider crystal phase. Fig. 6 presents the SEM image and EDS analysis of the machined surface. The element composition and proportion of the white phase marked I and the black phase marked II were collected by the point analysis of EDS. Obviously, black phases are rich in aluminum. The content of aluminum in black phase is about 93.5%, which is much higher than that in white phase about 60%. On the contrary, the content of Mg, Zn and Cu in black phase is much less than that of white phase

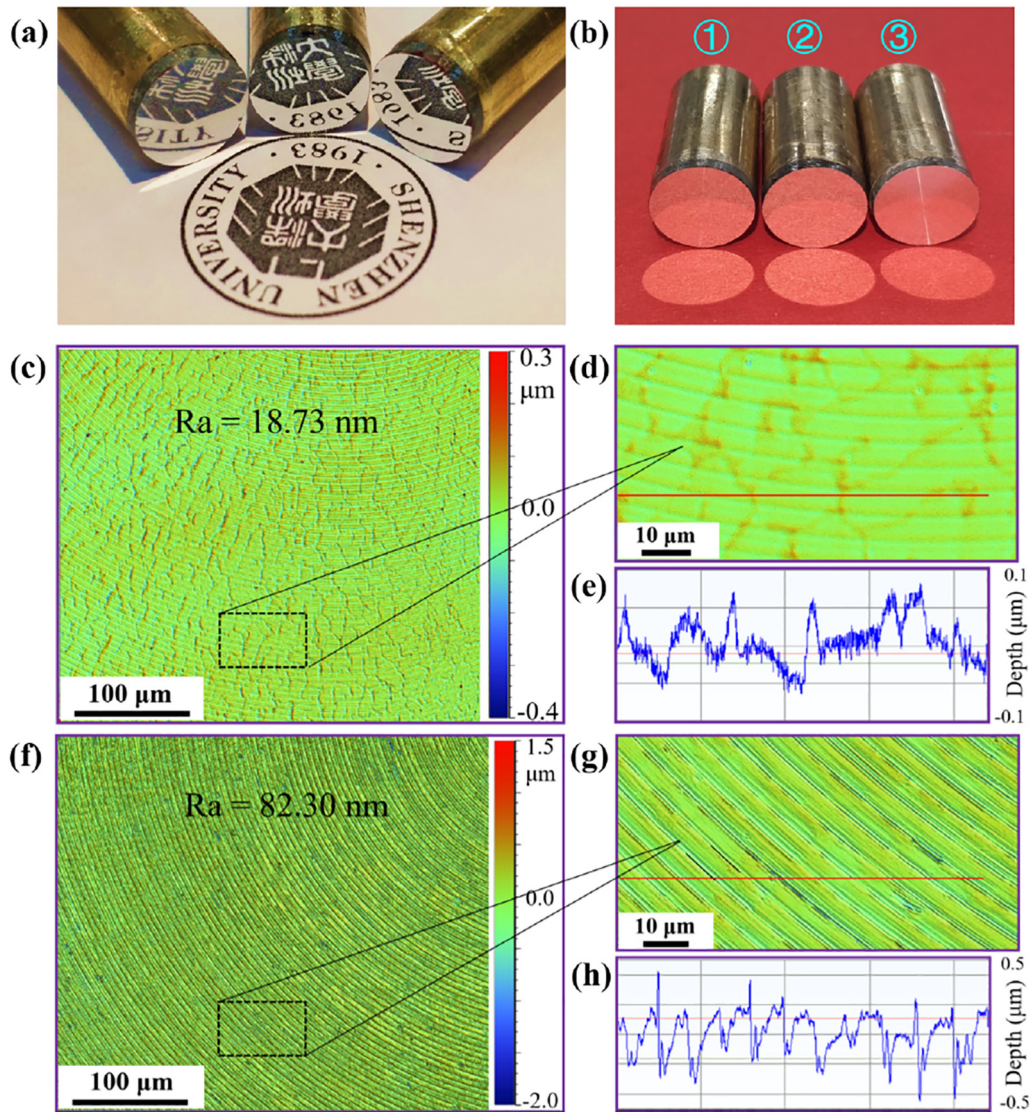


**Fig. 3.** (a) (b) The physical picture of sample surface after ultra-precision cutting. (c)–(h) the finished surface morphology and roughness of  $\text{Al}_{80}\text{Li}_5\text{Mg}_5\text{Zn}_5\text{Cu}_5$  workpieces measured by white light interferometer: (c) (f) surface morphologies cut by diamond tool and PCBN tool respectively. (d) (g) surface morphology local enlargement maps. (e) (h) roughness variation on a surface line. All the above sample processing parameters are:  $v = 2000$  r/min,  $f = 5$   $\mu\text{m}/\text{r}$ ,  $d = 8$   $\mu\text{m}$ .

(Fig. 6(b) and (d)). It can be deduced the black phase is FCC  $\alpha$ -Al phase, while white phase is Al/Al<sub>2</sub>Cu/MgZn<sub>2</sub> quaternary eutectic phase [23]. It can be seen from the SEM images (Fig. 6(a) and (c)) that the  $\text{Al}_{80}\text{Li}_5\text{Mg}_5\text{Zn}_5\text{Cu}_5$  HEA is mainly made up of two phases. The HEA has a dendrite casting structure, which is separated by a network structure between dendrites. Fine white network of Al/Al<sub>2</sub>Cu/MgZn<sub>2</sub> quaternary eutectic phase are formed on the surface of the sample, and homogeneously distributed in localized regions of the surface microstructure. The crystalline phase in the black region is surrounded by the white network eutectic phase. Cracks also appear in these white regions as shown in Fig. 6, suggesting the eutectic phase is the more brittle phase than FCC  $\alpha$ -Al phase, it also proves the existence of MgZn<sub>2</sub> phase which improves the hardness of eutectic phase [24]. This trend is probably caused by the inhomogeneous distribution of Zn, which precipitates from Al and contributes to the formation of the Al/Al<sub>2</sub>Cu/MgZn<sub>2</sub> quaternary eutectic phase. By comparing the surface morphology of the sample cut by diamond tool (Fig. 6(a)) with that of the sample cut by PCBN tool (Fig. 6(c)), it can be found that the area of white phase in Fig. 6a is smaller than that in Fig. 6(c). Because the eutectic phase has superplastic deformation ability, the white eutectic phase deforms more violently under

the action of greater friction force on the sample surface. It can also be inferred that PCBN tool has large friction force with the sample surface than diamond tool in the cutting process.

When the cutting volume of material is  $V_p$ , the expression of energy consumption is as follows [21]:

$$E_p = \sigma_y V_p \alpha h_m^3 \quad (2)$$

where  $h_m$ ,  $\sigma_y$  and  $E_p$  are the undeformed chip thickness, yield strength and energy consumption. According to Eq. (2) and the minimal energy principle analysis, when the two-phase material undergoes cutting deformation, the phase with lower strength will preferentially undergo larger plastic deformation to consume cutting power. According to the EDS analysis of machined surface of HEA, the content of aluminum in FCC  $\alpha$ -Al phase is about 30% higher than that in the Al/Al<sub>2</sub>Cu/MgZn<sub>2</sub> quaternary eutectic phase, and the corresponding strength is lower than that of eutectic phase. Therefore, the  $\alpha$ -Al phase on the machined surface of HEA will be extruded and stretched, plastic deformation occurs into a slender shape inducing the volume of the  $\alpha$ -Al phase decreases greatly. From the chip morphology analysis as shown in Fig. 6

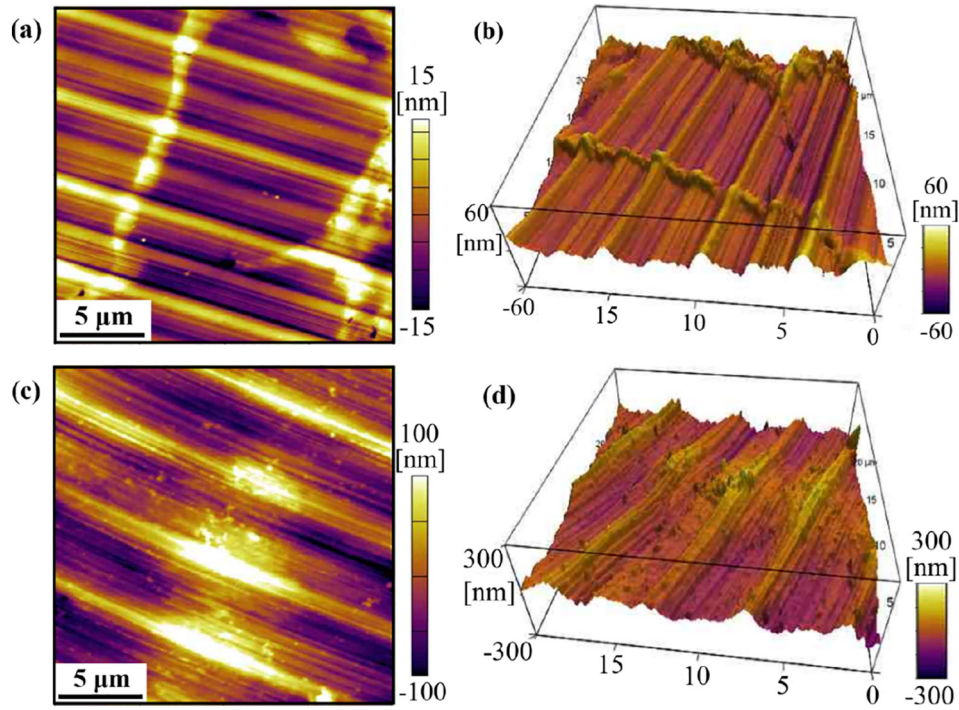


Fig. 4. AFM images (20 μm × 20 μm) of the surface machined: (a) (b) cut by diamond tool. (c) (d) cut by PCBN tool ( $v = 2000$  r/min,  $f = 5$  μm/r,  $d = 8$  μm).

(e) and (f), with the same tool geometry and cutting parameters as shown in Table 1, the chip shapes cut by diamond tool and PCBN tool look different. The inner surface of the chip cut by the diamond tool is subjected to the extrusion and friction of the cutting edge and flows out of rake surface, making the chip inner surface to be smoother. And the outer surface of the chip appears to be hairy due to the reversely curling and plastic deformation as shown in Fig. 6(e). However, the inner surface of the chip cut by the PCBN tool has a remarkable lamellar fold. This can be explained that the small radius of chip curvature in the cutting area, which causes the locally large deformation of the chip, including the chip to be pressed into a flat and thin layer, when the

bending stress exceeds the limit of material strength, the chip layer will break and enter a new deformation cycle along with the tool cutting motion, which will cause the periodic wrinkles on the chip surface and form intermittent cracks in the middle of the chip as shown in Fig. 6(f). This will affect the stability of the shear slip of the material in the cutting area and the machined surface roughness. To sum up, the PCBN tool has greater extrusion friction force than diamond tool in cutting HEA. Therefore, PCBN tool has more eutectic phase deformation on the machined surface of HEA, which reduces the proportion of FCC α-Al phase on the machined surface and leads to the increase of Al/Al<sub>2</sub>Cu/MgZn<sub>2</sub> quaternary eutectic phase on the machined surface.

Fig. 7 shows the EDS area analysis for the Al<sub>80</sub>Li<sub>5</sub>Mg<sub>5</sub>Zn<sub>5</sub>Cu<sub>5</sub> surface after the diamond tool and PCBN tool cutting, it can be seen that the actual atomic percentage of elements is close to that of the theory, the white phase is mainly the enrichment area of Mg, Zn, Cu and Al element, while the black phase is mainly Al element which was the primarily solidified α-Al phase.

### 3.3. Tool wear and mechanical property

Fig. 8(a) and (b) show the morphologies of PCBN tool and diamond tool after ultra-precision cutting. The images show that the diamond tool has little wear, while the PCBN cutting tool has a slight wear, because the new crystal phase appears on the tool surface, and it has a negative effect on the tool wear. The more phase transfer to the flank face and cutting edge of PCBN tool, the more serious the tool wear. The material removal and chipping process in cutting zone of ultra-precision turning are shown in Fig. 9. The undeformed chip thickness of materials in ultra-precision machining can be expressed as follows:

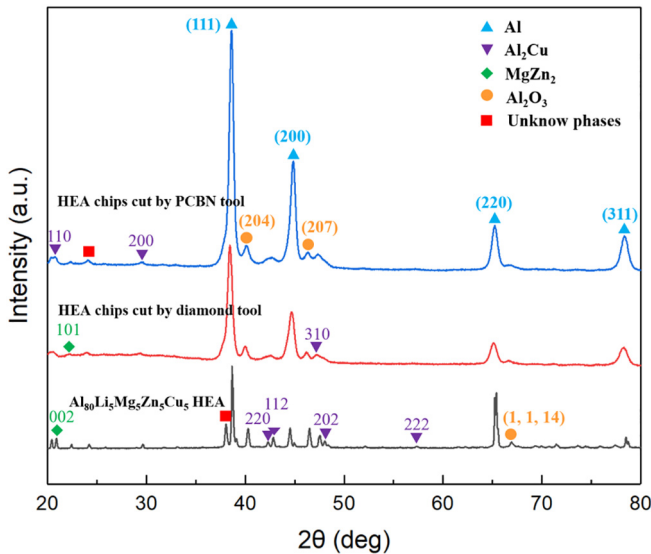
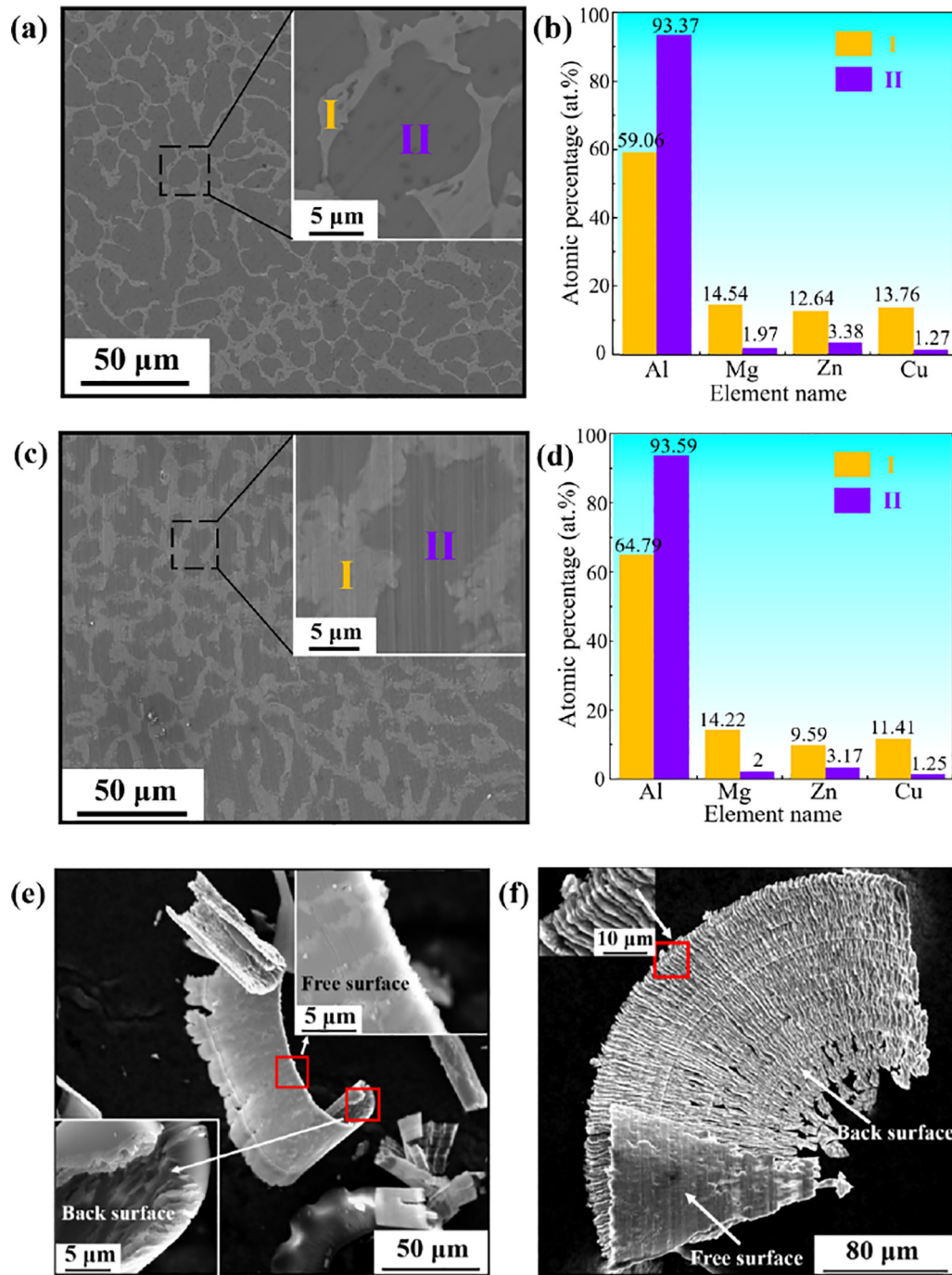


Fig. 5. XRD patterns of Al<sub>80</sub>Li<sub>5</sub>Mg<sub>5</sub>Zn<sub>5</sub>Cu<sub>5</sub> high-entropy alloy raw material, the diamond tool cutting chip and PCBN tool cutting chip.

$$\begin{cases} h_m = f \sin(\kappa_r) \\ \kappa_r = (\pi - \varepsilon_r) / 2 + \theta \end{cases} \quad (3)$$

where  $\kappa_r$ ,  $\varepsilon_r$  and  $\theta$  are the cutting edge angle, tool tip angle and the angle of tool feed. When the feed rate of ultra-precision cutting HEA is 5 μm/r, the dimension of undeformed chip thickness of HEA is similar to the



**Fig. 6.** SEM image and EDS analysis of the machining surface: (a) (c) machined surface by diamond tool and PCBN tool cutting respectively. (b) (d) atomic percentages of constituent elements in phase I and phase II of (a) (c). (e) chip morphology of HEA by diamond tool cutting. (f) chip morphology of HEA by PCBN tool cutting.

rounded cutting edge radius. Therefore, near the rounded cutting edge radius in the ultra-precision cutting area, the actual rake angle of material cutting is negative as shown in Fig. 9 and can be expressed as the following formula:

$$\alpha_c = \arcsin(1 - f \sin k_r / R_e) \quad (4)$$

Due to the existence of negative cutting rake angle, there will be a significant size effect in the material cutting process, which affects the material removal mechanism and the chip formation. Elastic-plastic deformation occurs in the cutting area when the material is extruded and sheared by the cutting edge. The crystalline phases of the HEA are

deformed under the extrusion and shearing of the cutting tool, and are removed by plastic ploughing.

Based on the above analysis, diamond tool and PCBN tool produce different chip shapes as shown in Fig. 6(e) and (f). The chip integrity cut by diamond tool is better, the reason may be that the friction coefficient of the contact extrusion between the chip outflow and the rake face of the tool is smaller than that of the PCBN tool. As a result, diamond tool is subject to more shear force, while PCBN tool is subject to greater extrusion force, which will produce different morphology and crystalline phase distribution in finished surface. The machined surface quality of the HEAs is closely related to the surface conditions of cutting tool. From SEM images, it shows that the surface of diamond tool is smoother

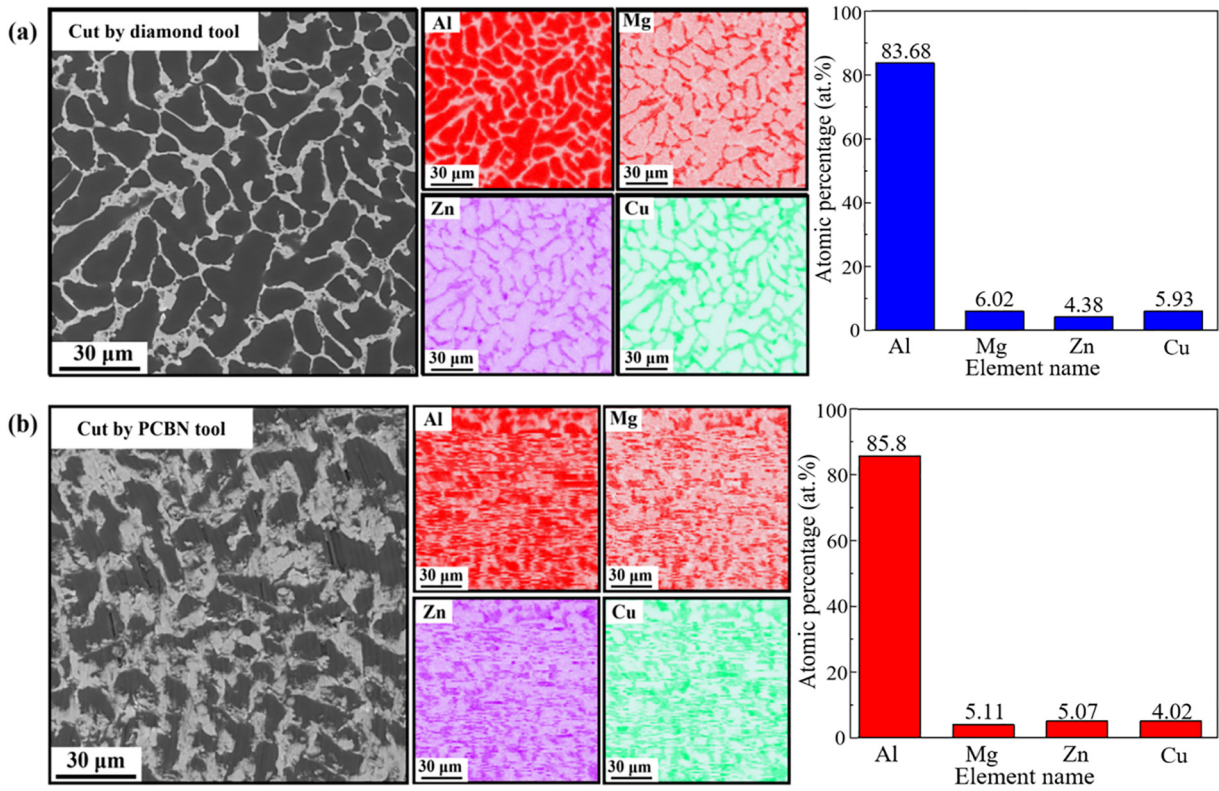


Fig. 7. SEM and EDS analysis for the  $Al_{80}Li_5Mg_5Zn_5Cu_5$  cutting surface: (a) cut by diamond tool (b) cut by PCBN tool ( $v = 2000$  r/min,  $f = 5 \mu\text{m}/r$ ,  $d = 8 \mu\text{m}$ ).

than that of PCBN tool. In the process of cutting HEA, the friction force and the extrusion force between the diamond tool surface and the surface of  $Al_{80}Li_5Mg_5Zn_5Cu_5$  is smaller, it can be proved from the morphology and deformation of cutting chips in Fig. 6.

In order to explore the effect of different cutting mechanism of diamond tool and PCBN tool on the mechanical properties of the finished surface, the microhardness of HEA surface was measured by microhardness tester. Fig. 10 shows the hardness change of HEA after ultra-precision cutting with different cutting tools. The raw material is polished by 2000 mesh sandpaper. The hardness values along one end of the surface diameter to the other end were collected by microhardness tester. The calculated average hardness value of the raw material is 211 HV. Then, the raw material was cut by diamond tool, the cutting parameters are:  $v = 2000$  r/min,  $f = 5 \mu\text{m}/r$ ,  $d = 8 \mu\text{m}$ . Using the above method to collecting hardness, the calculated average hardness value of HEA is down to 191 HV (Fig. 10). Finally, under the same cutting

parameters, PCBN tool was used to cut the same sample surface. The calculated average hardness value of HEA is 218 HV. Because the value of indentation depth is greater than the surface roughness value, although the surfaces roughness is different, it has little effect on microhardness measurement and the obtained microhardness value is reliable.

The change of hardness is mainly due to the different cutting mechanisms of these two tools in ultra-precision cutting HEA. The formation of chip morphology as shown in Fig. 6(f) shows that the material surface cut by PCBN tool is subjected to a large extrusion and friction during processing, which refines and diffuses the grains in the white phase region (Fig. 6). These increase and refinement eutectics of Al,  $Al_2Cu$  and  $MgZn_2$  have led to a more significant work-hardening and the substantial increase in hardness. Fig. 6(e) shows a relatively smooth chip surface, the extrusion force and friction force between material and tool are small. It indicates that the diamond tool is more obviously affected by shear force, so the hardness is down to 190 HV after the removal of

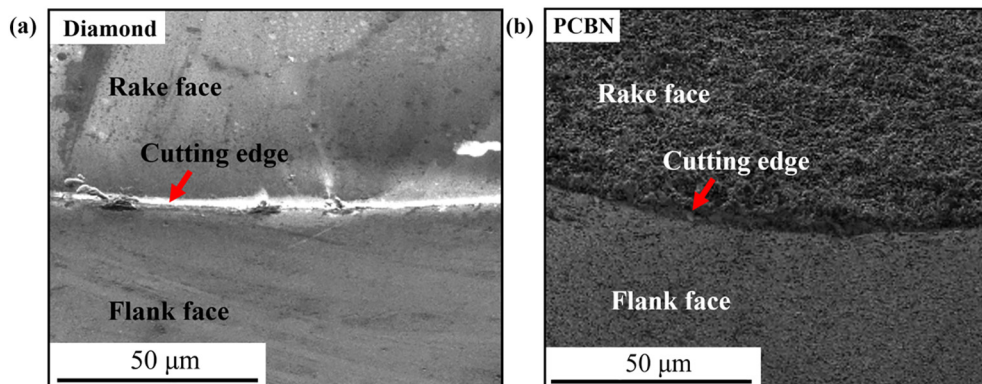


Fig. 8. SEM images of cutting tool morphology and wear: (a) diamond tool. (b) PCBN tool.

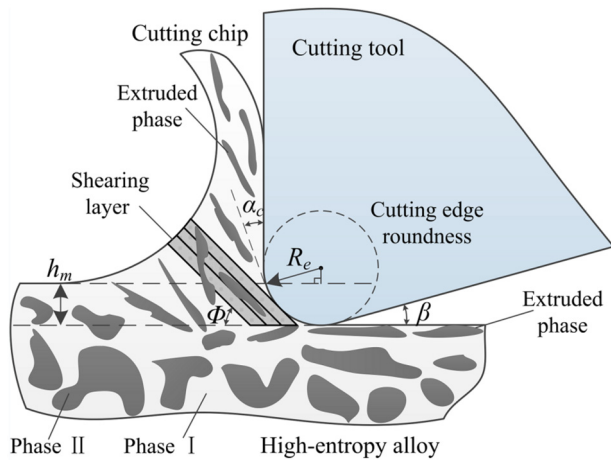


Fig. 9. Material removal and chipping process in cutting zone of ultra-precision cutting ( $v = 2000$  r/min,  $f = 5$   $\mu$ m/r,  $d = 8$   $\mu$ m).

the hardened layer of raw material, meanwhile the better finished surface of HEA (Fig. 2(a)) and the more distinct grains (Fig. 6(a)) with small deformation were obtained.

#### 4. Conclusions

- (i) With the increase of ultra-precision cutting parameters, the surface roughness value of  $\text{Al}_{80}\text{Li}_5\text{Mg}_5\text{Zn}_5\text{Cu}_5$  high-entropy alloy increases, and the feed rate has the greatest influence on the surface roughness, followed by the cutting depth, while the spindle speed has no significant influence on surface roughness. The  $R_a$  value cut by diamond tool ranges from 10 nm to 20 nm with little change, while the surface cut by PCBN tool shows a clear upward trend with the parameter increases and the  $R_a$  value ranges from 40 nm to 120 nm. The results show that diamond tool has better cutting effect than PCBN tool.
- (ii) The EDS analysis shows that the elements on the machined surface are evenly distributed. Under the observation of SEM and the analysis of XRD, obviously, the machining surface of HEA appears the primarily solidified  $\alpha$ -Al phase and quaternary eutectic phase of Al,  $\text{Al}_2\text{Cu}$  and  $\text{MgZn}_2$ .

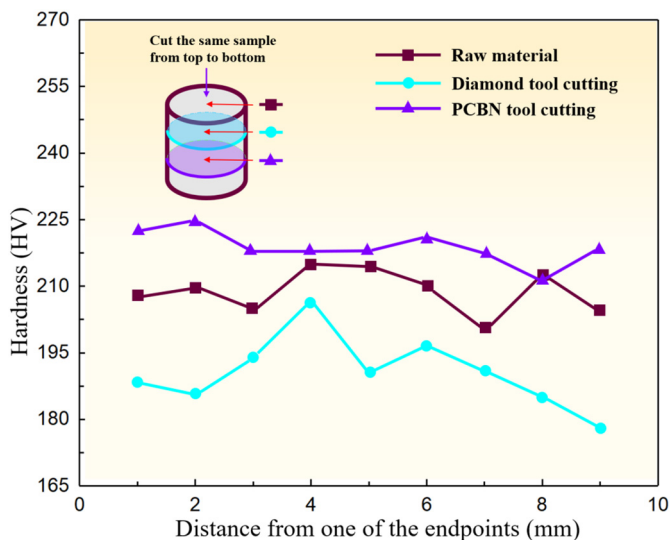


Fig. 10. Hardness value of material surface by 2000 mesh sandpaper polishing, diamond tool cutting and PCBN tool cutting respectively ( $v = 2000$  r/min,  $f = 5$   $\mu$ m/r,  $d = 8$   $\mu$ m).

- (iii) The cutting mechanism of  $\text{Al}_{80}\text{Li}_5\text{Mg}_5\text{Zn}_5\text{Cu}_5$  HEA is analyzed by corresponding chip morphology. The results indicate that when the PCBN tool is used to cut the HEA, it produces greater extrusion and friction between the tool and the HEA surface, which makes the eutectic phase diffuse and refine. Due to the large extrusion force and friction force between the PCBN tool and the HEA surface in the process of cutting, the hardness of finished surface is increased to 218 HV. Compared with PCBN tool cutting, diamond tool cutting is more affected by shear force, and its hardness down to 190 HV. At the same time, shear force is also one of the reasons for the lower surface roughness.

#### CRedit authorship contribution statement

**Zhiyuan Huang:** Conceptualization, Writing - original draft, Investigation. **Yuqi Dai:** Investigation, Data curation. **Zhen Li:** Writing - original draft, Formal analysis. **Guoqing Zhang:** Formal analysis, Resources. **Chuntao Chang:** Formal analysis, Supervision, Resources. **Jiang Ma:** Conceptualization, Supervision, Resources, Writing - review & editing.

#### Declaration of competing interest

There are no conflicts to declare.

#### Acknowledgements

This work was supported by the National Key Research and Development Program of China (Grant No. 2018YFA0703604), the NSFC (Nos. 51871157), the Science and Technology Innovation Commission Shenzhen (Nos. JCYJ20170412111216258), the postgraduate innovation development fund project of Shenzhen University (Nos. PIDFP-ZR2019012). The authors wish to acknowledge the assistance on microscope observation received from the Electron Microscope Center of the Shenzhen University.

#### References

- [1] J.W. Yeh, S.K. Chen, S.J. Lin, J.Y. Gan, T.S. Chin, T.T. Shun, C.H. Tsau, S.Y. Chang, Nano-structured high-entropy alloys with multiple principal elements: novel alloy design concepts and outcomes, *Adv. Eng. Mater.* 6 (5) (2004) 299–303.
- [2] J.M. Wu, S.J. Lin, J.W. Yeh, S.K. Chen, Y.S. Huang, H.C. Chen, Adhesive wear behavior of Al x CoCrCuFeNi high-entropy alloys as a function of aluminum content, *Wear* 261 (5) (2006) 513–519.
- [3] Q. Ding, Y. Zhang, X. Chen, X. Fu, D. Chen, S. Chen, L. Gu, F. Wei, H. Bei, Y. Gao, M. Wen, J. Li, Z. Zhang, T. Zhu, R.O. Ritchie, Q. Yu, Tuning element distribution, structure and properties by composition in high-entropy alloys, *Nature* 574 (7777) (2019) 223.
- [4] A. Raza, H.J. Ryu, S.H. Hong, Strength enhancement and density reduction by the addition of Al in CrFeMoV based high-entropy alloy fabricated through powder metallurgy, *Mater. Des.* 157 (2018) 97–104.
- [5] W. Huo, H. Zhou, F. Fang, Z. Xie, J. Jiang, Microstructure and mechanical properties of CoCrFeNiZrx eutectic high-entropy alloys, *Mater. Des.* 134 (2017) 226–233.
- [6] Y. Zou, P. Okle, H. Yu, T. Sumigawa, T. Kitamura, S. Maiti, W. Steurer, R. Spolenak, Fracture properties of a refractory high-entropy alloy: in situ micro-cantilever and atom probe tomography studies, *Scr. Mater.* 128 (2017) 95–99.
- [7] P. Sathiyamoorthi, J. Basu, S. Kashyap, K.G. Pradeep, R.S. Kottada, Thermal stability and grain boundary strengthening in ultrafine-grained CoCrFeNi high entropy alloy composite, *Mater. Des.* 134 (2017) 426–433.
- [8] F. Otto, Y. Yang, H. Bei, E.P. George, Relative effects of enthalpy and entropy on the phase stability of equiatomic high-entropy alloys, *Acta Mater.* 61 (7) (2013) 2628–2638.
- [9] Y.S. Huang, L. Chen, H.W. Lui, M.H. Cai, J.W. Yeh, Microstructure, hardness, resistivity and thermal stability of sputtered oxide films of AlCoCrCu 0.5 NiFe high-entropy alloy, *Mater. Sci. Eng. A* 457 (1) (2007) 77–83.
- [10] B. Gludovatz, A. Hohenwarter, D. Catoor, E.H. Chang, E.P. George, R.O. Ritchie, A fracture-resistant high-entropy alloy for cryogenic applications, *Science* 345 (6201) (2014) 1153.
- [11] T. Egami, M. Ojha, O. Khorgolkhuu, D.M. Nicholson, G.M. Stocks, Local electronic effects and irradiation resistance in high-entropy alloys, *JOM* 67 (10) (2015) 2345–2349.
- [12] K.Y. Tsai, M.H. Tsai, J.W. Yeh, Sluggish diffusion in Co–Cr–Fe–Mn–Ni high-entropy alloys, *Acta Mater.* 61 (13) (2013) 4887–4897.

- [13] S. Huang, L. Wei, L. Song, F. Tian, S. Jiang, E. Holmström, L. Vitos, Temperature dependent stacking fault energy of FeCrCoNiMn high entropy alloy, *Scr. Mater.* 108 (2015) 44–47.
- [14] W. Zhang, P.K. Liaw, Y. Zhang, Science and technology in high-entropy alloys, *Sci. China Mater.* 61 (2018) 2–22.
- [15] S.G. Ma, P.K. Liaw, M.C. Gao, J.W. Qiao, Z.H. Wang, Y. Zhang, Damping behavior of Al x CoCrFeNi high-entropy alloys by a dynamic mechanical analyzer, *J. Alloys Compd.* 604 (9) (2014) 331–339.
- [16] G. Zhang, S. To, X. Wu, Y. Lou, Steady tool wear and its influence on tool geometry in ultra-precision fly cutting of CuZn30, *Int. J. Adv. Manuf. Technol.* 1–4 (2018) 1–10.
- [17] Z. Zhu, S. To, W.-L. Zhu, P. Huang, X. Zhou, Cutting forces in fast-/slow tool servo diamond turning of micro-structured surfaces, *Int. J. Mach. Tools Manuf.* 136 (2019) 62–75.
- [18] R. Wang, Y. Tang, S. Li, H. Zhang, Y. Ye, L.a. Zhu, Y. Ai, S. Bai, Novel metastable engineering in single-phase high-entropy alloy, *Mater. Des.* 162 (2019) 256–262.
- [19] J. Zhang, T. Cui, C. Ge, Y. Sui, H. Yang, Review of micro/nano machining by utilizing elliptical vibration cutting, *Int. J. Mach. Tools Manuf.* 106 (2016) 109–126.
- [20] X. Chen, J. Xiao, Y. Zhu, R. Tian, X. Shu, J. Xu, Micro-machinability of bulk metallic glass in ultra-precision cutting, *Mater. Des.* 136 (2017) 1–12.
- [21] T.G. Bifano, T.A. Dow, R.O. Scattergood, Ductile-regime grinding: a new technology for machining brittle materials, *J. Eng. Ind.* 113 (2) (1991) 184–189.
- [22] R. Li, Z. Wang, Z. Guo, P.K. Liaw, T. Zhang, L. Li, Y. Zhang, Graded microstructures of Al-Li-Mg-Zn-Cu entropic alloys under supergravity, *Sci. China Mater.* 62 (2019) 736–744.
- [23] X. Yang, S.Y. Chen, J.D. Cotton, Y. Zhang, Phase stability of low-density, multiprincipal component alloys containing aluminum, magnesium, and lithium, *JOM* 66 (2014) 2009–2020.
- [24] N. Takata, T. Okano, A. Suzuki, M. Kobashi, Microstructure of intermetallic-reinforced Al-based alloy composites fabricated using eutectic reactions in Al-Mg-Zn ternary system, *Intermetallics* 95 (2018) 48–58.